PIV Study of Small-Scale Flow Structure around a Rushton Turbine

K. V. Sharp and R. J. Adrian
Dept. of Theoretical and Applied Mechanics, University of Illinois at Urbana-Champaign, Urbana, IL 61801

The structure of turbulent motions was measured in a region surrounding the blade tips of a Rushton turbine mixer. The tip vortices responsible for micromixing were created in this region, as was the radial jet that drives the large-scale circulation responsible for macromixing. Measurements of instantaneous velocity fields in axial−radial planes showed large cycle-to-cycle variability relative to the mean. The average measurements of the azimuthal vorticity and the Reynolds stresses in the radial−axial plane showed the growth and motion of the tip vortices as they drift away from the blades. Radial and axial spatial derivatives were measured to assess various methods of computing the turbulent viscous dissipation. The small scales were significantly anisotropic at the Reynolds numbers studied.

Introduction

Stirred-tank reactors, consisting of a radial or axial turbine rotating in a cylindrical chamber, are commonly used in industrial applications. The mixing process is difficult to measure and quantify, and scaling is not reliable, partly because mixing mechanisms are not well understood. Micromixing occurs on the smallest scales, and thus it is enlightening to study the structures and statistics at such scales. If we consider the energy-cascade model proposed by Kolmogorov (Hunt et al., 1991), energy is transported from the larger eddies to the smaller eddies and dissipated on the smallest scales. In mixing tanks, however, the rotating blades add energy at a scale that is significantly smaller than the scale of the large recirculations, that is, the middle of the energy spectrum. This study elucidates some of the small-scale characteristics and structures of flow around a Rushton turbine by performing two-dimensional field measurements in the $r-z$ plane using particle image velocimetry (PIV). Estimates of local turbulent dissipation, ϵ, are also presented.

According to Kresta (1998):

“Specification of the local dissipation is one of the keys to successful process modeling for blend time (at least in jet mixers), drop break-up (for a fixed liquid-liquid system), reactor design (where the limiting time scale is the micromixing time scale, not the kinetics), cell damage (where there is no bubble bursting at the surface), and in some aspects of crystallization, gas dispersion, and flocculation.”

The distributions of local dissipation and root mean square (rms) velocities are also of fundamental importance to turbulence modelers. Yet the direct measurement of fully resolved instantaneous spatial velocity gradients needed to measure ϵ has not yet been achieved experimentally.

Dynamics of the bulk flow around a Rushton turbine have been documented by Desouza and Pike (1972), Yianneskis et al. (1987), Ducoste and Clark (1997), and Schäfer et al. (1996). It is on this scale that “macromixing” is caused by large-scale ring vortices with length scales of the order of half the tank diameter. Desouza and Pike (1972) depict the impeller flow as a high-speed jet, entraining flow with increasing r, and producing a flow at the wall resembling a stagnation point flow. At the wall, the jet splits and heads upwards and downwards along the wall before the separate streams circulate back toward the impeller. This circulation is often described as a large-scale ring vortex. Flow visualization of this ring vortex can be found in Yianneskis et al. (1987). Figure 1 shows the flow structure, including the radial jet, the large-scale ring vortices, and the shed tip vortices in the impeller region.

Mean velocity-field measurements in the impeller region around a Rushton turbine have been documented by numer-

---

Correspondence concerning this article should be addressed to K. V. Sharp.
Present address of K. V. Sharp: Dept. of Theoretical and Applied Mechanics, 216 Talbot Laboratory, 104 South Wright Street, University of Illinois, Urbana, IL 61801.

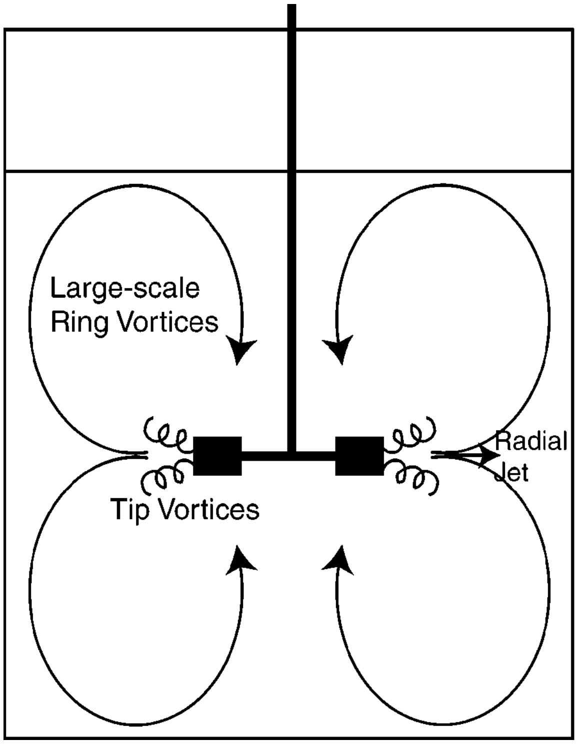

Figure 1. Flow, including radial jet, large-scale ring vortices, and tip vortices.

ous authors, including Stoots and Calabrese (1995), Yianneskis et al. (1987), Yianneskis and Whitelaw (1993) and Rutherford et al. (1996). Stoots and Calabrese (1995) also introduced a quantity δ^*, characterizing "a measure of the magnitude of the deformation rate due to mean velocity gradients in the flow field."

The structure and trajectory of the tip vortices (trailing-edge vortices) have been investigated by Van't Riet et al. (1975), Yianneskis et al. (1987), and Stoots and Calabrese (1995), among others. These studies primarily used single-point measurement techniques and photographic velocity techniques for visualization.

PIV was used to investigate the bulk flow around a pitched-blade turbine (PBT) by Sheng et al. (1998) and Bakker et al. (1996). These measurements were focused on the larger-scale structures rather than the small-scale structures in the impeller region.

Using PIV to investigate the small-scale structures, we not only obtain instantaneous field information for velocity, but also obtain field information for rms velocities, and vorticity of the small scales. The structure of the instantaneous velocity field shows strong tip vortex coherence even 50° past blade passage. This result is not apparent when examining mean field data, as the cycle-to-cycle variability is masked significantly by the averaging process. Vorticity and Reynolds stress measurements are generally difficult, if not impossible, to obtain using single-point measurement techniques. The present measurements of the spatial *distribution* of vorticity and rms velocities in the impeller region are emphasized.

Turbulent dissipation in a stirred mixer has been measured by Kresta and Wood (1993), Wu and Patterson (1989), Rao and Brodkey (1972), Cutter (1966), Okamoto et al. (1981), and Komasawa et al. (1974), among others. A number of methods have been used in estimating turbulent dissipation. The majority of measurements until now have used single-point techniques to obtain velocities and spectra in these systems. Due to the presence of the blade, there is a periodic component to the flow in the stirred tank. Both Wu and Patterson (1989) and Kresta and Wood (1993) considered the effects of this "pseudoturbulence" on the measurement of dissipation, though Kresta and Wood's work used a PBT rather than a Rushton turbine. The direct calculation of turbulent dissipation rate is not yet fully attainable, as this would require fully three-dimensional instantaneous measurements with extremely high spatial resolution. But, estimates employing direct velocity gradient information are offered, and the effects of the method of velocity decomposition are compared. The isotropy of the turbulence at the measured spatial resolution is assessed.

Experimental Apparatus and Procedure

The six-bladed symmetric Rushton turbine has a nominal diameter, D, of 50.8 mm, tip to tip (Figure 2a). Figure 2b shows the mixer and tank configuration. The inner diameter

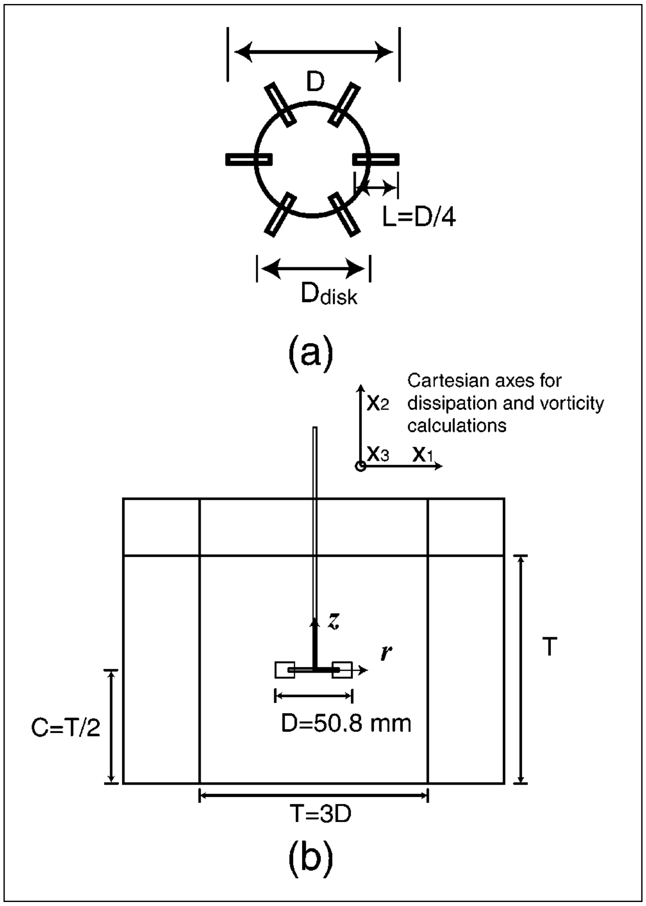

Figure 2. (a) Rushton turbine geometry; (b) dimensional relationships among blade diameter, filled-tank depth, turbine clearance, and tank diameter.

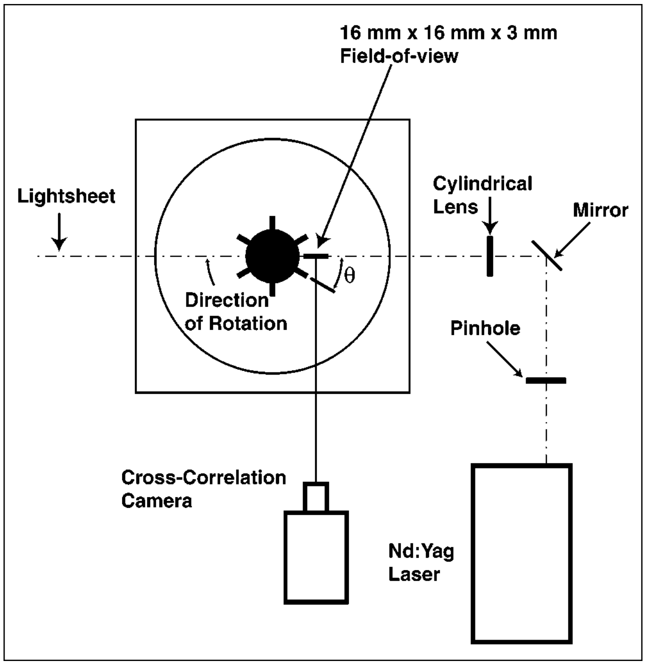

Figure 3. Top view of experimental apparatus, including tank, blade, lightsheet, measurement volume, and definition of degrees past blade passage, θ.

of the tank, T, is equal to $3D$. The depth of deionized water in the cylinder was also T. To minimize optical distortion at the curved surface, the cylindrical test section was contained in a rectangular box, and the space between the cylinder and the outer walls was also filled with water. The clearance, C, between the vertical center of the turbine and the bottom of the tank was $T/2$.

Although the velocity data are presented in cylindrical coordinates $(r-z)$, it is useful to employ Cartesian coordinates for calculation of vorticity and dissipation in a particular plane. For example, to calculate the out-of-plane vorticity at a given $r-z$ plane using Cartesian coordinates and indicial notation, one can set the directions as follows: $1=r$, $2=z$, and $3=$ out-of-plane. For this particular plane, the 3-component thus corresponds directly to the circumferential component, and using Cartesian formulation for vorticity or dissipation simplifies the calculations.

A standard 1K×1K TSI PIV 10-30 cross-correlation CCD camera was used to record the PIV images. A New Wave Nd:Yag Mini-Lase provided a maximum energy of 50 mJ per pulse. The lightsheet was carefully aligned such that it was parallel with the z-axis and centered between the front and the back of the test section (Figure 3). Images were acquired at six different blade positions, or six different values of θ, referring to Figure 3. Since the turbine is symmetric in 60° increments, data were acquired for only one sextant. Within this sextant, $r-z$ plane images were acquired at $\theta=0°$ (along the center line of the blade), $\theta=10°$, $\theta=20°$, $\theta=30°$, $\theta=40°$, and $\theta=50°$. Two hundred images were acquired at each angular blade position. The laser pulse is extremely short, of the order of 10 ns, so the blade turns less than $6.0*10^{-6}$ degrees during each individual image acquisition. The time between pulses, Δt, is of the order 600 μs, so the blade turns approximately 0.36 degree during the acquisition of a pair of images. This defines the angular resolution. Since two-frame cross-correlation techniques were applied during interrogation, the 200 frames yielded 100 vector fields at each location.

The actual dimensions of the Rushton turbine used in the experiment were measured with a standard caliper. The mean tip-to-tip diameter, D, measured within 0.2% of the nominal 2 in. (50.8 mm), with a standard deviation of 0.2%. The rectangular blade width, L, measured within 0.8% of its nominal $D/4$, and the blade height, W, measured within 2.5% of its nominal $D/5$. The mean blade thickness measured 0.0962 in.

Images were initially acquired for two differing fields of view, namely, 34.4 mm by 34.7 mm (magnification = 1.12) and 16.1 mm by 16.2 mm (magnification = 0.56). Previous calculations suggest that the first, and lesser-resolved, dataset underestimates the velocity gradients. Details of these calculations and comparisons can be found in Sharp et al. (1998). In the current article, all of the data were acquired in the smaller window. For high-quality PIV images, the maximum displacement of the particles in the cross-correlated images should be less than one-quarter of the lightsheet thickness and/or the interrogation spot size (Keane and Adrian, 1992). In a radial turbine flow, such as the one under consideration, the significant out-of-plane motion dominates, so following the "one-quarter" rule for the out-of-plane motion automatically satisfies the in-plane constraint. Thus the time between pulses, Δt, was optimized to allow for the largest $r-z$ pixel displacement possible without the loss of too many particles out of the $r-z$ plane between laser pulses.

Bakker et al. (1996) and Sheng et al. (1998) used PIV to investigate the flow in tanks stirred by a PBT; however, these measurements focused more on the large-scale flow than the details of the flow in the impeller region. In both cases, the lightsheet was 10 mm thick, the tank had a diameter of 0.292 m, and the field-of-view encompassed the whole flow field, necessitating low spatial resolution. For example, the measurements in Sheng et al. (1998) have a quoted resolution of roughly 5 mm or 1.7% of the tank diameter. The grid spacing in the current study is approximately 0.165% of the tank diameter, approximately 10 times smaller. But, to obtain this resolution, the field-of-view had to be restricted to 16 mm by 16 mm.

TSI Insight 2.0 software was used to interrogate the images with two-frame cross-correlation between 32-pixel-by-32-pixel windows and 50% overlap between interrogation windows. The distance between sampled vectors is 0.255 mm in the r- and z-directions. Following interrogation, the images were ported to the CLEANVEC program (Soloff and Meinhart, private communication, 1998) for postprocessing, which included removing spurious vectors, replacing them if appropriate and painting out the region of the field of view blocked by the projection of the blade in the plane of the lightsheet.

The elevation of the free surface varied within 3 mm for the 100-rpm revolution speed used for all measurements. The density, ρ, and kinematic viscosity, ν, of the water was 997.4 kg/m^3 and $0.936*10^{-6}$ m^2/s, respectively. The turbulence microscale (λ) computed from the radial velocity, u_r'', and its radial derivative, $u''_{r,r}$,

$$\lambda = \sqrt{\frac{\overline{u_r''^2}}{\overline{u_{r,r}''^2}}} \tag{1}$$

was approximately 1.1 mm. The turbulent Reynolds number,

$$Re_\lambda = \frac{\sqrt{\overline{u_r''^2}}\,\lambda}{\nu} \tag{2}$$

is approximately 54. $N_{Re} = \rho N D^2/\mu$ is 4580, where $N =$ revolutions per second, and $\mu =$ viscosity of the fluid. The power number, $N_p = P/\rho N^3 D^5$ is 4.5. The mean turbulent dissipation, $\bar{\epsilon}$, is calculated to be 0.0025 m^2/s^3 from:

$$\bar{\epsilon} = \frac{P}{\rho V}, \tag{3}$$

where P is the power input to the flow, and V represents the volume of water in the test section. The choice of N_{Re} was limited at the upper end since, as N_{Re} increases, so does the free-surface variation and at some point, cavitation is introduced into the system. The selection of N_{Re} = 4580 represented the highest rotation rate that could be obtained with minimal free-surface variation.

Results

Influence of periodic blade passage: definition of turbulent velocities

In determining the turbulence statistics of this flow, previous investigations have generally employed one of two approaches to the periodic component. The periodic component can be removed from the calculation of turbulence statistics, as done by Wu and Patterson (1989), or not (Rao and Brodkey, 1972; Komasawa et al., 1974; Okamoto et al., 1981). The primary question of interest here is whether or not the tip vortices and the periodic flow associated with blade passage can be treated simply as large turbulent eddies that follow Kolmogorov's energy cascade theory, dissipating their energy in the smallest scales, or if these periodic disturbances need to be considered as a separate component of the flow. Define the instantaneous (total) velocity field by $\tilde{u}$, the periodic wave by u_p, the conditionally averaged velocity given the blade position by $\langle \tilde{u} | \theta \rangle$, the unconditionally time-averaged velocity by $\langle \tilde{u} \rangle$, and the fluctuating velocity by u'. When defined using a traditional Reynolds averaged approach, the fluctuating velocity is:

$$u' \equiv \tilde{u} - \langle \tilde{u} \rangle. \tag{4}$$

Using, instead, Reynolds and Hussain's (1972) triple decomposition for examining turbulence in the presence of a periodic wave flow, the turbulent motion is defined as

$$u'' \equiv \tilde{u} - \langle \tilde{u} | \theta \rangle, \tag{5}$$

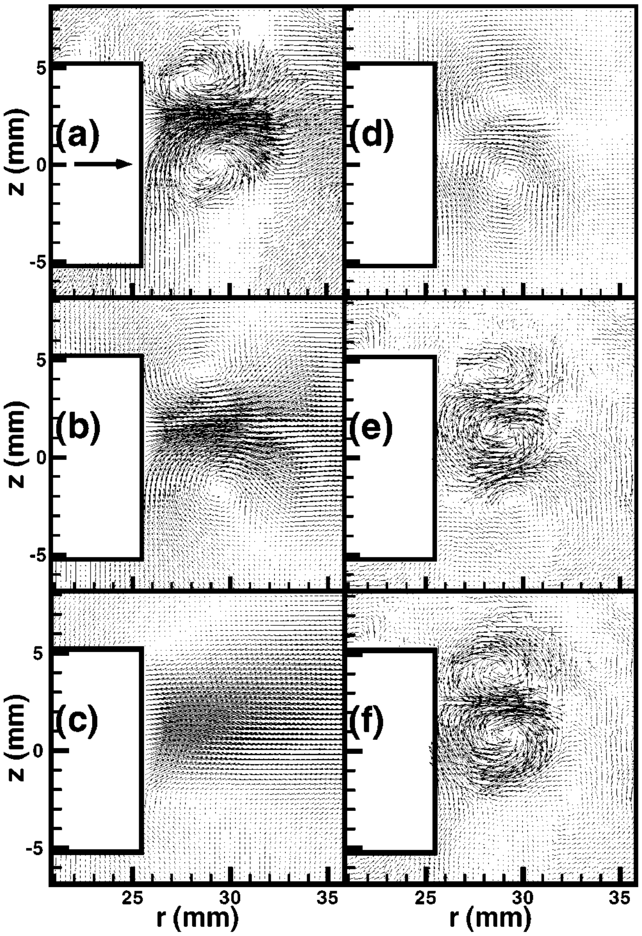

Figure 4. Velocity fields, average and fluctuating, for visualizing the two methods of decomposition.

(a) Typical instantaneous velocity vector field at 30 degrees past blade passage, $\tilde{u}$; (b) phase-averaged velocity field, $\langle \tilde{u} | \theta \rangle$; (c) mean velocity field, averaged over all blade positions, $\langle \tilde{u} \rangle$; (d) periodic component determined by Eq. 6, u_p; (e) fluctuating velocity as defined by triple decomposition (Eq. 5), u''; (f) fluctuating velocity as defined by standard RANS decomposition (Eq. 4), u'.

where the periodic component is defined as

$$u_p \equiv \langle \tilde{u} | \theta \rangle - \langle \tilde{u} \rangle. \tag{6}$$

Hence

$$u'' = u' - u_p \tag{7}$$

is the fluctuation with the periodic component removed.

In this study, turbulence statistics are calculated using both the RANS decomposition (Eq. 4) and the triple decomposition of Reynolds and Hussein (1972) (Eq. 5).

For a visual example of the velocity decompositions, typical velocity fields in Figure 4 illustrate the difference between subtracting the phase-averaged mean, $\langle \tilde{u} | \theta \rangle$, and subtracting the mean flow, $\langle \tilde{u} \rangle$. The effects of the different methods of decomposition on statistical quantities are addressed in the Discussion section.

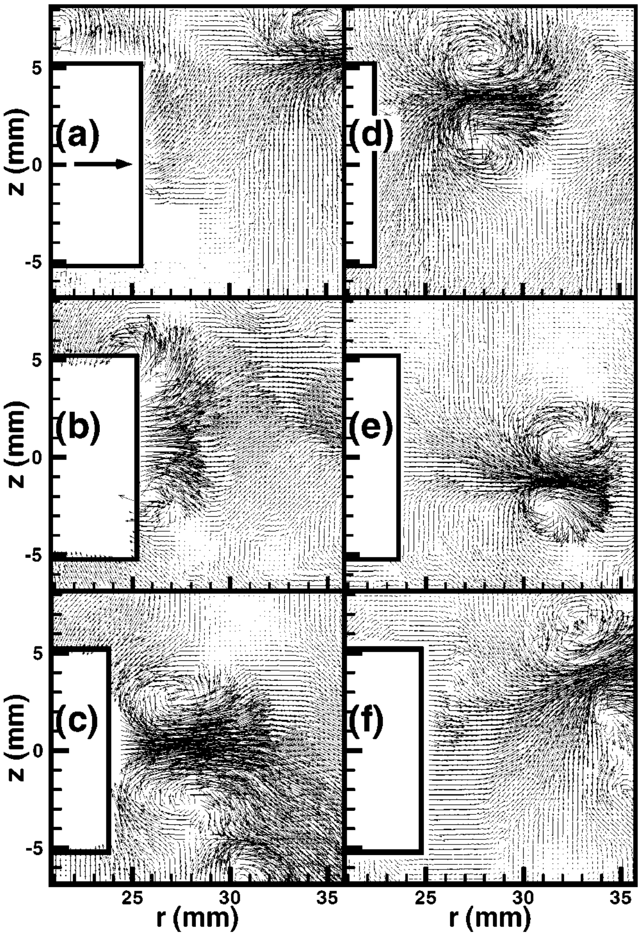

Figure 5. Typical instantaneous velocity fields, $\tilde{u}$, measured during different revolutions of the blade.

The locations of the measurement plane, in degrees past blade passage, are as follows: (a) 0°, (b) 10°, (c) 20°, (d) 30°, (e) 40°, and (f) 50°. The reference vector in frame (a) has magnitude of the blade's tip velocity, V_{tip}.

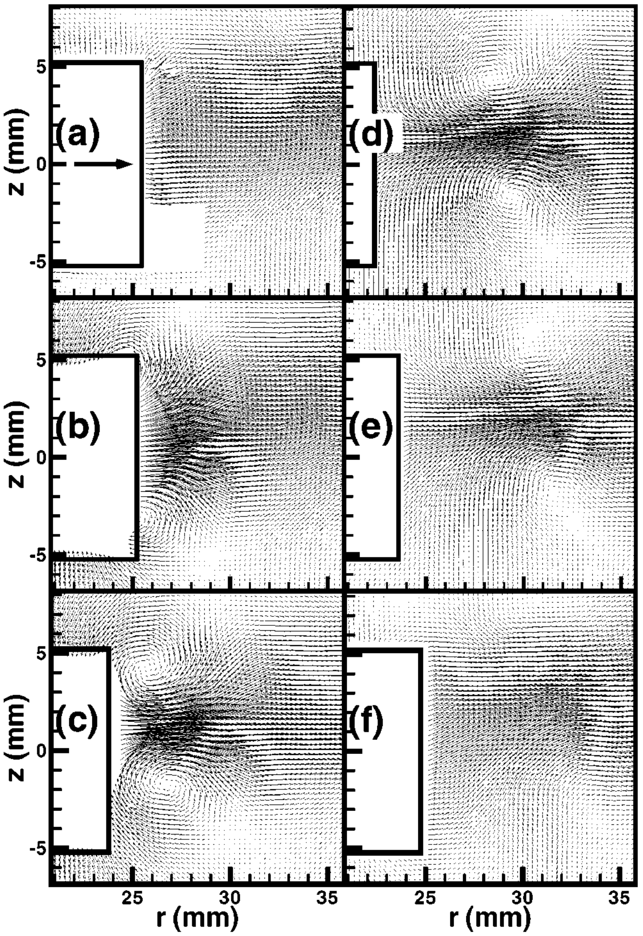

Figure 6. Series of phase-averaged velocity fields, $\langle \tilde{u} | \theta \rangle$.

The locations of the measurement plane, in degrees past blade passage, are as follows: (a) 0°, (b) 10°, (c) 20°, (d) 30°, (e) 40°, and (f) 50°. The reference vector in frame (a) has magnitude of the blade's tip velocity, V_{tip}.

Velocity fields

The structure of the tip vortices is visualized at six stations between one set of blades, both instantaneously and in the mean. The instantaneous velocity fields, $\tilde{u}$, in Figure 5 are representative, but not sequential. The series of phase-averaged velocity fields, $\langle \tilde{u} | \theta \rangle$, in Figure 6 was found by averaging over 100 instantaneous velocity fields at each blade position.

Ideally, a larger ensemble would have been used to ensure statistical convergence, but it was not feasible to do so. The statistical convergence has been assessed by considering the statistics of an ensemble of 50 vector fields vs. an ensemble of 100 vector fields in a plane 20 degrees past blade passage and in the region close to the blade containing the tip vortex. If the pixel displacements are on the order of several pixels, as they are in the vicinity of the tip vortices (also the region of highest vorticity and dissipation), the differences in calculation of mean and rms velocities between 50-frame and 100-frame ensembles are less than 3%. In the direction of highest velocity, for example, in the radial direction in the radial jet structure, the differences in calculation of mean and rms velocities between 50-frame and 100-frame ensembles is less than 1%. Thus, although larger ensembles would be ideal, the statistics calculated using ensembles of 100 frames are converged to within a few percent.

It is instructive to compare the instantaneous views of the tip vortices and radial jet flow to the properties inferred in earlier studies of the mean flow (Yianneskis et al., 1987; Stoots and Calabrese, 1995; Rutherford et al., 1996). The axial trajectories of the vortices found in the mean flow studies differ considerably from those observed in the instantaneous velocity fields. Specifically, the tip vortices do not consistently convect upwards or downwards in each cycle in Figure 5. Rather, they convect in either direction, depending upon the cycle. In the mean, these differences average out and the vortices appear to convect radially with minimal (but observable) movement in the axial direction (Figure 6). The contrast between the mean and instantaneous fields, and the magnitude of the cycle-to-cycle variation are shown in Figure 7, where three instantaneous velocity fields are compared to the mean field (averaged over 100 instantaneous realizations) for a radial-axial plane 30 degrees past blade passage. Similarly, Fig-

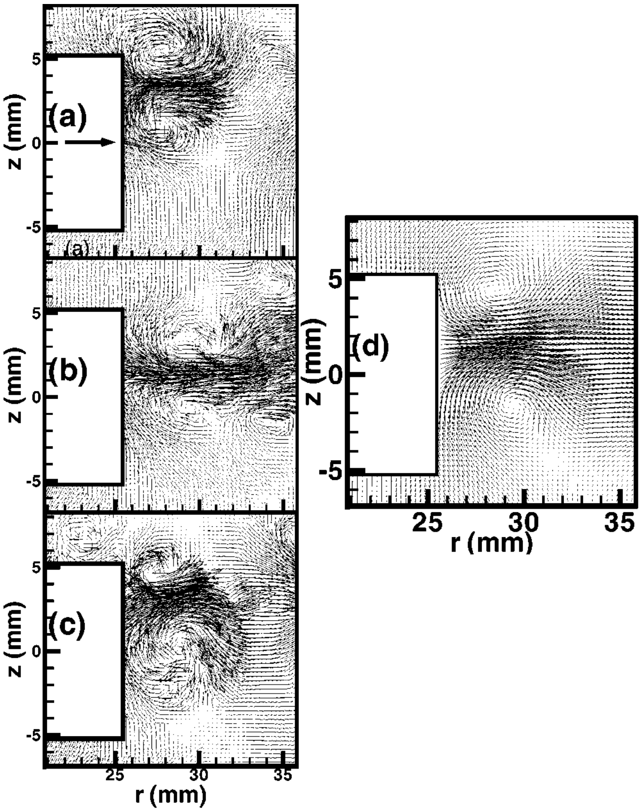

Figure 7. Cycle-to-cycle variability in a plane 30 degrees past blade passage.

(a), (b), and (c) are instantaneous vector fields, $\tilde{u}$, at $\theta = 30°$, and (d) is $\langle \tilde{u} | \theta = \mathbf{30°} \rangle$, ensemble-averaged over 100 velocity fields.

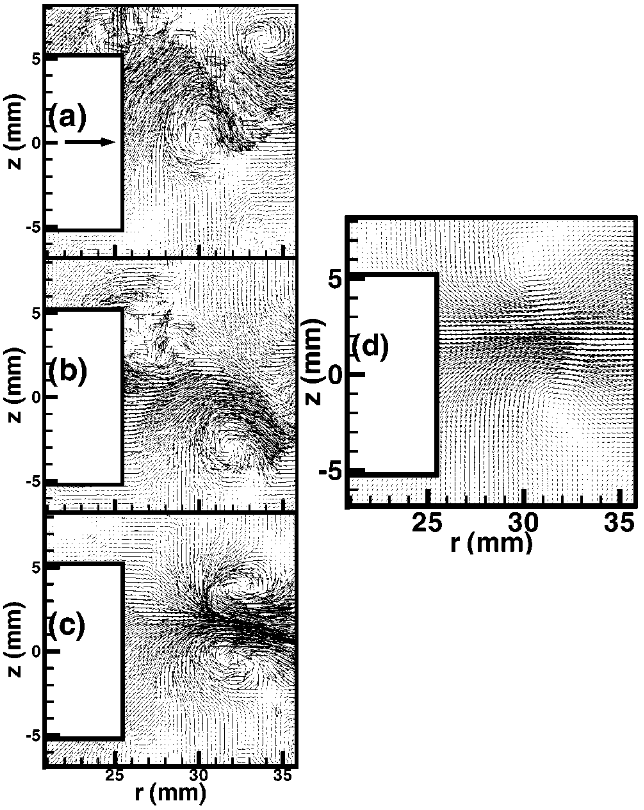

Figure 8. Cycle-to-cycle variability in a plane 40 degrees past blade passage.

(a), (b), and (c) are instantaneous vector fields, $\tilde{u}$, at $\theta = 40°$, and (d) is $\langle \tilde{u} | \theta = \mathbf{40°} \rangle$, ensemble-averaged over 100 velocity fields.

ure 8 shows velocity fields for a radial−axial plane 40 degrees past blade passage.

The phase-averaged azimuthal vorticity fields ($\langle \omega_3 | \theta \rangle$) averaged over 100 instantaneous realizations are shown in Figure 9. Similarly, data are presented for the normalized rms radial velocities in Figure 10, the normalized rms axial velocities in Figure 11, and the normalized Reynolds stresses in Figure 12. The principal conclusions drawn from these results are that the small-scale tip vortices, and the associated radial jet are responsible for most of the vorticity and turbulent Reynolds stresses in this region. Note the strong correlation between the mean patterns of $u_r''^2$, $u_z''^2$, and ω_3, where ω_3 is defined as:

$$\omega_3 = \frac{\partial \tilde{u}_2}{\partial x_1} - \frac{\partial \tilde{u}_1}{\partial x_2}, \tag{8}$$

directions: $1 = r$, $2 = z$, $3 =$ azimuthal.

Dissipation Results

Methods for calculating dissipation using PIV data

The rate of dissipation of scalar concentration fluctuations, ϵ_c, is effectively a measure of the rate of mixing. In the analysis of turbulent mixing, it is sometimes conjectured that ϵ_c is proportional to ϵ, the rate of viscous dissipation of mechanical energy in turbulent motions.

In terms of the spatial gradients, the latter is

$$\epsilon = \nu \Big\{ 2\Big(\overline{u_{1,1}^2} + \overline{u_{2,2}^2} + \overline{u_{3,3}^2} \Big) + \overline{u_{1,2}^2} + \overline{u_{2,1}^2} + \overline{u_{1,3}^2} + \overline{u_{3,1}^2} + \overline{u_{2,3}^2} + \overline{u_{3,2}^2} + 2\Big(\overline{u_{1,2}u_{2,1}} + \overline{u_{1,3}u_{3,1}} + \overline{u_{2,3}u_{3,2}} \Big) \Big\}, \tag{9}$$

where u_i denotes a turbulent fluctuation, either u_i' or u_i'', depending on the meaning one attaches to ϵ. Using PIV measurements in the $r-z$ plane, one is able to calculate 5 of the 12 terms, namely $\overline{u_{1,1}^2}$, $\overline{u_{1,2}^2}$, $\overline{u_{2,1}^2}$, $\overline{u_{2,2}^2}$, and $\overline{u_{1,2}u_{2,1}}$, where $1 = r$, $2 = z$ and 3 represents the circumferential direction (see Figure 2b for axis notation). Knowledge of these components allows for several estimates of dissipation to be calculated, relying upon assumptions of statistical isotropy or statistical axisymmetry.

The following estimates are presented: (a) ϵ_i, fully isotropic estimate depending only on $\overline{u_{1,1}^2}$; (b) ϵ_{ii}, estimate using all measured gradients and statistically isotropic assumptions for the unmeasured components; (c) ϵ_{axi-1}, estimate assuming statistical axisymmetry about the 1-axis (r); and (d) ϵ_{axi-2}, estimate assuming statistical axisymmetry about the 2-axis (z). The normalized local dissipation, ϵ^*, is defined as the local dissipation divided by the tank-averaged dissipation, where $\bar{\epsilon}$ is given by Eq. 3.

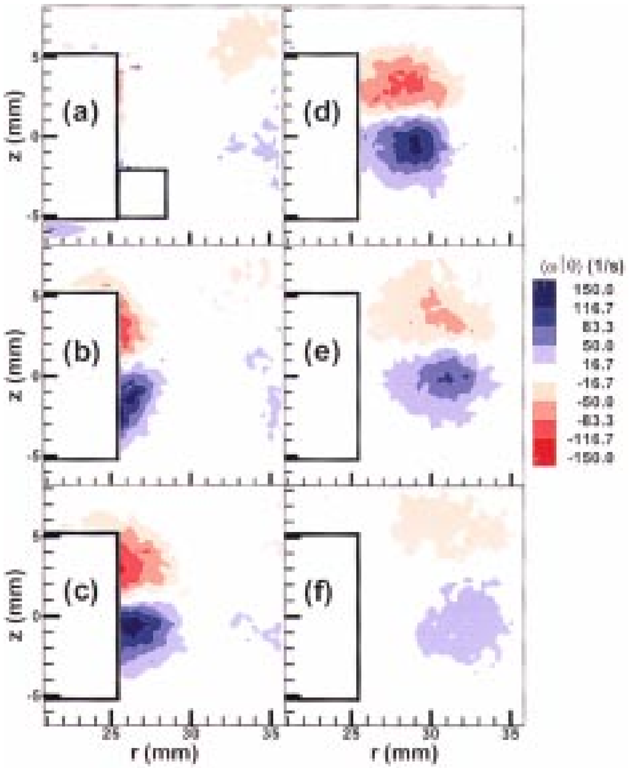

Figure 9. Contours of mean azimuthal vorticity, $\langle \omega_3 | \theta \rangle$, contours vs. blade position.

The locations of the measurement plane, in degrees past blade passage, are as follows: (a) 0°, (b) 10°, (c) 20°, (d) 30°, (e) 40°, and (f) 50°.

Details of the various approximations for ϵ can be found in Sharp et al. (1999). For reference, the equations are:

$$\epsilon_i = 15\nu\overline{u_{1,1}^2} \tag{10}$$

$$\begin{aligned}\epsilon_{ii} = \nu\Bigg\{ & 2\left(\overline{u_{1,1}^2} + \overline{u_{2,2}^2} + \frac{1}{2}\left(\overline{u_{1,1}^2} + \overline{u_{2,2}^2}\right)\right) \\ & + \overline{u_{1,2}^2} + \overline{u_{2,1}^2} + 2\left(\overline{u_{1,2}^2} + \overline{u_{2,1}^2}\right) \\ & + 2\left(\overline{u_{1,2}u_{2,1}}\right) - \left(\overline{u_{1,1}^2} + \overline{u_{2,2}^2}\right)\Bigg\}\end{aligned} \tag{11}$$

$$\epsilon_{axi-1} = \nu\left(-\overline{u_{1,1}^2} + 2\overline{u_{1,2}^2} + 2\overline{u_{2,1}^2} + 8\overline{u_{2,2}^2}\right) \tag{12}$$

$$\epsilon_{axi-2} = \nu\left(-\overline{u_{2,2}^2} + 2\overline{u_{2,1}^2} + 2\overline{u_{1,2}^2} + 8\overline{u_{1,1}^2}\right). \tag{13}$$

Distribution of dissipation

Figure 13 compares two estimates of dissipation, each calculated using either the RANS decomposition ($u = u'$ in Eqs. 10–13) or the triple decomposition ($u = u''$ in Eqs. 10–13). The results show that the removal of the periodic component does not significantly affect the calculation of turbulence quantities, which is in full agreement with the results of Kresta and Wood (1993) for a PBT. Thus, for at least two blade types, the impact of the periodic component of velocity is much less significant than the assumptions employed in calculating the estimates.

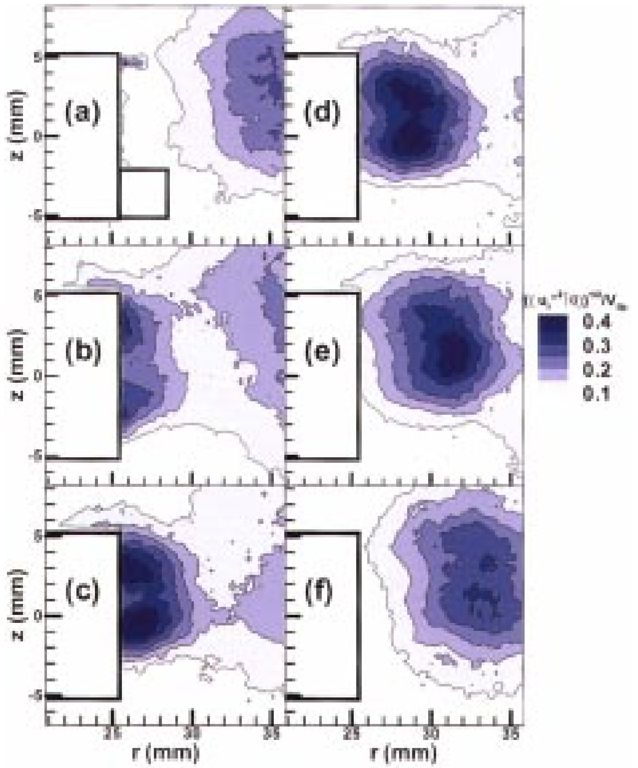

Figure 10. Contours of phase-averaged rms radial velocity, $(\langle u_r''^2 | \theta \rangle)^{1/2}$, normalized by V_{tip}.

The locations of the measurement plane, in degrees past blade passage, are as follows: (a) 0°, (b) 10°, (c) 20°, (d) 30°, (e) 40°, and (f) 50°.

Figure 14 shows the normalized dissipation, ϵ^*, found from Eq. 11 and employing triple decomposition ($u = u''$ in Eq. 11). The variation of our dissipation results associated with the different methods of calculation is $\pm 30\%$. This is smaller than the spread in the data from other experiments, although differences in geometry and Reynolds number between these experiments are responsible for some of this variation. The degree to which small scales are isotropic is assessed directly in Figures 15 and 16. Ratios of mean square gradients should all be equal to one if the isotropic assumptions were fully valid for the small scales of this flow. Clearly, this is not the case for the Reynolds numbers under consideration.

Discussion

Velocity fields

In previous studies, the existence of tip vortices shed by the blades of the Rushton turbine has been inferred from single-point measurements and standard photographic visualization. Although cycle-to-cycle variability has been recognized (Yianneskis and Whitelaw, 1993), the coherence of the tip vortices traveling radially from the blade has not been documented. Using single-point data, Yianneskis and Whitelaw (1993) found evidence that "a vortical pattern was present at all times up to 20° behind each blade." In the instantaneous velocity vector fields in Figure 5, tip vortices are evident even at 50 degrees past blade passage.

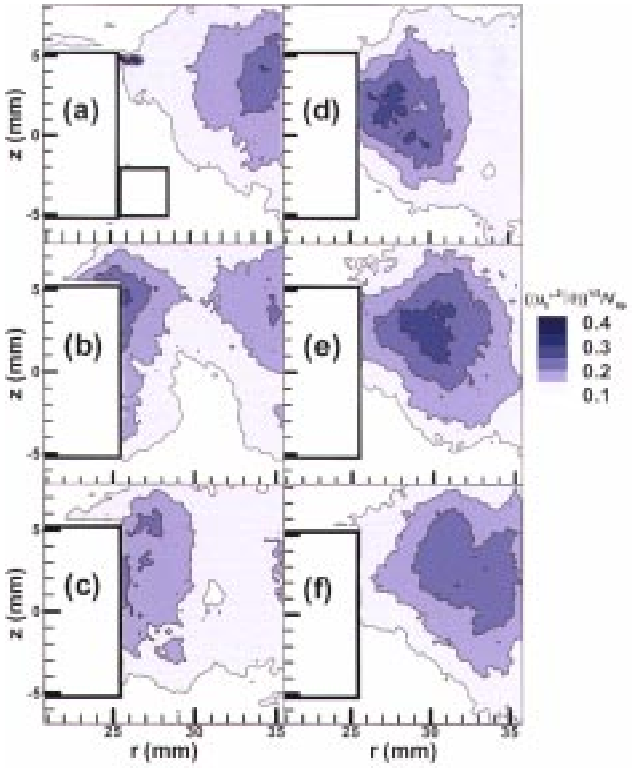

Figure 11. Contours of phase-averaged rms axial velocity, $(\langle u_z''^2 | \theta \rangle)^{1/2}$, normalized by V_{tip}.

The locations of the measurement plane, in degrees past blade passage, are as follows: (a) 0°, (b) 10°, (c) 20°, (d) 30°, (e) 40°, and (f) 50°.

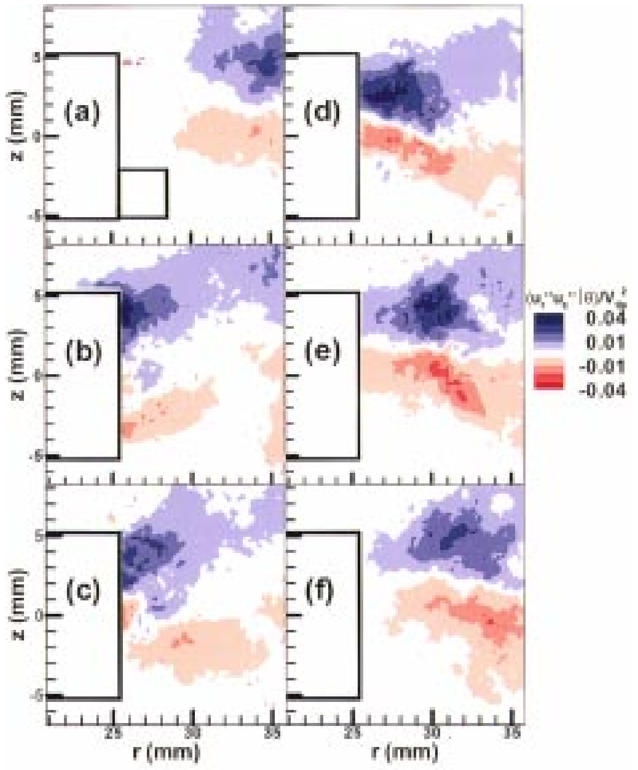

Figure 12. Contours of phase-averaged Reynolds stresses, $\langle u_r'' u_z'' | \theta \rangle$, normalized by V_{tip}^2.

The locations of the measurement plane, in degrees past blade passage, are as follows: (a) 0°, (b) 10°, (c) 20°, (d) 30°, (e) 40°, and (f) 50°.

Quantitative information on the instantaneous structure of the shed tip vortices has been obtained in this experiment. According to Yianneskis and Whitelaw (1993), axial velocity traces measured with an LDA probe at $r/R = 1.42$ and $z = 0.46H$, where H is the blade height, show that the motion is ''more erratic [than at positions closer to the blade]; most of the cycles recorded at that point did not exhibit any particular trends. This cycle-to-cycle variation of the velocities away from the blades indicated the break-up of the trailing vortex into smaller eddies.'' The instantaneous velocity fields in Figure 5 suggest that the erratic motion observed in Yianneskis and Whitelaw's (1993) velocity traces is more a function of the cycle-to-cycle variability of the tip vortex trajectory rather than a breakup of the vortex itself.

Figures 7 and 8 document the significant cycle-to-cycle variability in the trajectory, particularly in the axial direction. It is difficult to discern such instantaneous structures in the mean field measurements. Although the vertical position of the zero mean axial velocity component does not appear to vary with radius, the instantaneous location does, and both the magnitude of this movement and its direction vary between cycles. Thus, average fields lose much of the real physics. Some portion of this variation in trajectory might be attributable to shaft precession since, similarly to many previous studies (Yianneskis et al., 1987; Yianneskis and Whitelaw, 1993; Rutherford et al., 1996; Stoots and Calabrese, 1995), the end of the shaft is free. (The maximum precession of the tip of the shaft was less than ±0.5 mm.) However, the turbulent disturbances in which the tip vortices evolve create fluid displacements significantly larger than the motion of the shaft. Therefore, the cycle-to-cycle variability is not dominated by motion of the shaft. The plots of the rms velocities (Figures 10 and 11) show that in the near blade region, the magnitude of normalized rms velocities does not exceed 0.5. For these calculations, the fluctuating velocity did not include the periodic component and was defined by u'', Eq. 5. For $\theta = 30°$, similar calculations were done defining the fluctuating velocity, u', using a standard RANS formulation (Eq. 4). Area averaging over the field of view, the difference in radial and axial rms velocities using these two decompositions was approximately 10%. In regions close to the blade, the maximum variation in rms velocities was 50–60%, showing that the inclusion or exclusion of periodic velocity components has a significant effect close to the blade, but loses its impact quickly as the distance from the blade increases.

Figures 10, 11, and 12 reflect the structure of the tip vortices moving away from the blades. In particular, there is a strong correlation between the tip vortices, the vorticity, and the Reynolds stresses. As the vortices move outward, so do the regions of maximum stress. Thus, the energetic behavior of the turbulent motion is dominated by the tip vortices, which are midscale mechanisms. These data are useful for turbulence model predictions and are available on the Laboratory for Turbulence and Complex Flow (LTCF) Web site, as described in the Appendix.

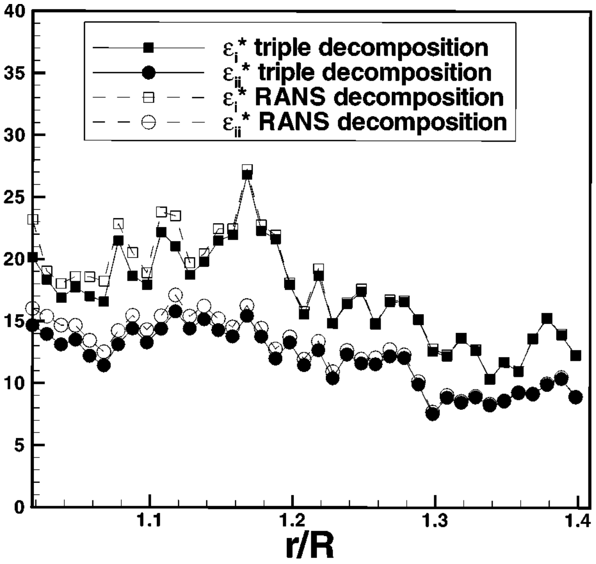

Figure 13. Normalized dissipation, ϵ^*, along $z = 0$ estimated from two forms of the isotropic equations.

The estimate is insensitive to the decomposition, showing that the periodic component dissipates little energy.

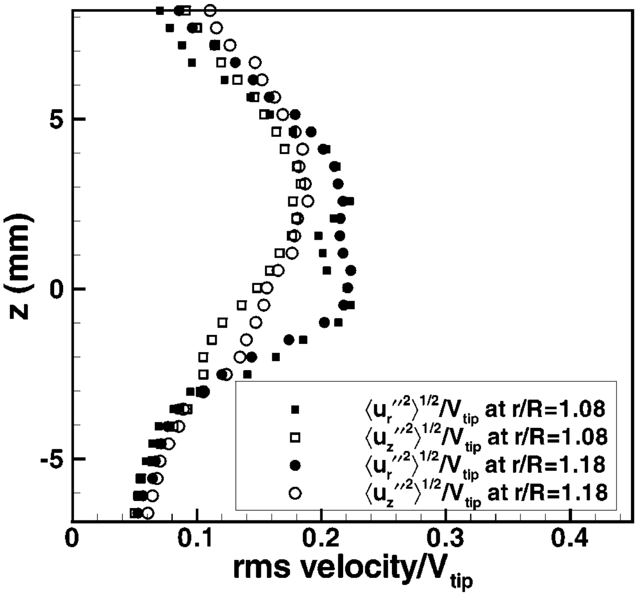

Figure 15. Rms components of velocity, $\langle u_r''^2\rangle^{1/2}$ and $\langle u_z''^2\rangle^{1/2}$, normalized by V_{tip}, and plotted at $r/R = 1.08$ and $r/R = 1.18$ vs. z; the blade is centered vertically about $z = 0$.

Dissipation

The calculation of turbulent dissipation in any given flow remains a challenge. In order to perform this calculation, single-point measurements rely on Taylor's hypothesis and assumptions of local isotropy in the form of $\epsilon = 15\nu\overline{\left[(\partial u_1/\partial x_1)^2\right]}$ or the equivalent spectral form $\epsilon = \nu\int k_1^2 E\, dk_1$; or they use the empirical relation $\epsilon = A(\overline{u^2})^{3/2}/L$, based on isotropic turbulence. PIV measures instantaneous *spatial* derivatives, but only some, not all. Hence it also assumes small-scale isotropy or an equivalent. Higher Reynolds number stirred flows may be more isotropic. With the significant

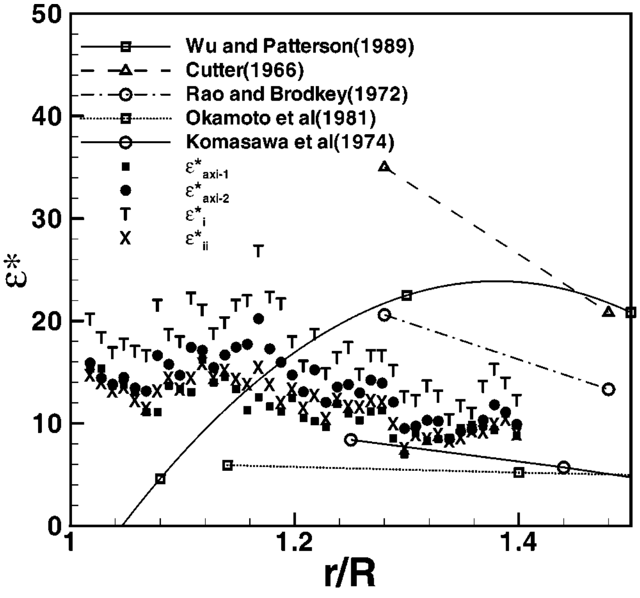

Figure 14. Normalized dissipation, ϵ^*, averaged over all blade positions, vs. r/R at the blade center line.

All of the calculations here were performed using the triple decomposition (Eq. 5). Results from other studies are included for reference, but comparison is limited by differences between the mixer/tank configuration and Reynolds numbers.

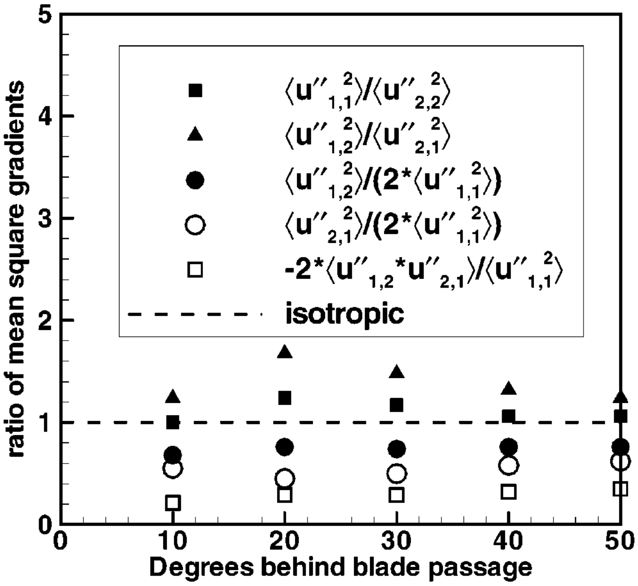

Figure 16. Comparison of isotropic assumptions for data processed using the triple decomposition (Eq. 5).

If the flow is fully isotropic, each ratio should be equal to one.

inhomogeneity of this type of flow, however, small-scale isotropy is not guaranteed even at higher Reynolds numbers.

Michelet et al. (1997) performed space−time correlations in the impeller stream to specifically assess the applicability of Taylor's hypothesis in a stirred-tank flow. In a highly three-dimensional flow such as a stirred tank, the definition of a convective velocity proves challenging. Michelet et al. (1997) concluded that the local mean velocity can be adequately used as the convection velocity for time separations less than the time macroscale and distances less than the macroscale, assuming that the effect of the inhomogeneity of the flow is taken into account. For larger times and distances, a correction was proposed. The important point here is that there are enough complicating factors in stirred-tank flow, namely anisotropy at large scales, inhomogeneity and periodicity due to the passage of the blades, that the assumptions used in estimating dissipation rates from single-point measurement techniques should be carefully assessed.

Wu and Patterson (1989) and Ducoste and Clark (1997) both estimated the local dissipation from single-point LDV data by using Taylor's hypothesis and different forms of the fundamental empirical relationship $\epsilon = Au^3/L$, where u is a root-mean-square velocity and L is a dissipation length scale, often approximated by an integral length scale. Wu and Patterson (1989) removed the periodic component and dealt with the anisotropy by averaging the integral scales found from the correlation function in three directions. Ducoste and Clark (1997) accounted for the varying direction of the mean field used in Taylor's hypothesis by using the rms of the velocity fluctuation in the direction of the local mean flow.

Rao and Brodkey (1972) used a three-dimensional pitot probe to determine the direction of the mean velocity at different points in the flow. A hot-film anemometer was then used to determine the magnitude of both the mean and the fluctuating velocities at these points. In order to calculate the local dissipation, the velocity microscale was obtained both directly from the derivative signal and from the velocity spectrum. Taylor's hypothesis was used to transform the time series into a space series. The dissipation was then calculated using the isotropic relation:

$$\epsilon = 15\nu\frac{\overline{u^2}}{\lambda^2}. \tag{14}$$

Okamoto et al. (1981) and Komasawa et al. (1974) calculated the dissipation from energy spectra measured using a hot-film current meter and cine-photography methods, respectively.

Another option for measuring local dissipation is to use a control volume approach, as in Gunkel and Weber (1975) and Cutter (1966), where the velocities were measured with a hot-wire anemometer and photographic method, respectively. Gunkel and Weber (1975) concluded that most of the energy dissipation occurs in the bulk flow of the tank, a conclusion that disagrees with Cutter (1966) as well as the current study.

Generally, it is assumed that in order to fully resolve the velocity scales in a turbulent flow, the measurement technique must be capable of resolving velocities down to a small multiple of the Kolmogorov microscale, $\eta = \{\nu^3/\epsilon\}^{1/4}$. While PIV solves the issue of measuring true spatial derivatives, as opposed to inferring them from time derivatives, it, along with other measurement techniques, still suffers from spatial resolution that may not be sufficient to fully resolve the Kolmogorov scale.

The spatial resolution of these PIV data is approximately 0.5 mm. Based upon the mean dissipation in the tank, the Kolmogorov scale is estimated at 0.14 mm. The dissipation in the impeller region is known to be considerably larger than the mean dissipation in the tank, so in order to be fully resolved in the impeller region, the spatial resolution should be better than 0.14 mm. Define the local normalized dissipation ϵ^* as $\epsilon/\bar{\epsilon}$, where ϵ is the local dissipation and $\bar{\epsilon}$ is the tank-averaged dissipation rate. If $\epsilon^* = 20$ near the impeller, η_{local} would be approximately half that of the η estimated using $\bar{\epsilon}$. Thus, the resolution in this study is 3.5 times the tank-averaged η and 7 times the local Kolmogorov scale. The local dissipation measurements in the impeller region appear well within the range measured in previous studies, but even so, we cannot guarantee *a priori* that the measurements are fully resolved. Instead, the measured fields are considered to be filtered velocity fields.

In Wu and Patterson's (1989) study, the LDV measurement volume was 0.5 mm in diameter and 1 mm in length, on the order of magnitude of the turbulence microscales. The dimensions of the LDV measuring volume in Ducoste and Clark (1997) were 143 μm diameter by 2.28 mm in length.

Kresta and Wood (1993) also used LDA, but to examine the flow around a PBT. The LDA measurement volume was 0.12 mm in diameter and 1.02 mm in length. Kresta and Wood (1993) acknowledge that it was not possible to measure the full frequency spectrum, since the Nyquist criterion would have required a frequency response of 8.8 kHz. Although data were acquired with a frequency of up to 11 kHz, most of the data were acquired in the 4−7-kHz range.

A number of methods of calculating the dissipation from single-point measurements were compared in Kresta and Wood (1993). Several methods of estimating dissipation from single-point measurements were not recommended for future calculations, including the application of Taylor's hypothesis to convert a time series to a space series. Concern was expressed over the frequency resolution of LDV measurements and the convergence of results using several sampling frequencies.

Sheng et al. (1998) also used PIV measurements to estimate dissipation in a stirred tank. Since the resolution of the velocity measurement was roughly 5 mm (or 50 times the estimated Kolmogorov scale in the given flow), the directly calculated velocity gradients are not suited to directly estimating dissipation. Dissipation results presented by Sheng et al. (1998) are thus based on a ''large eddy'' technique. The details of this calculation are not yet available.

The local dissipation in the impeller region, ϵ_{local} is much greater than the tank-averaged dissipation, $\bar{\epsilon}$. Figure 14 shows the variation in normalized dissipation, ϵ^*, with radial position. In this plot, the general trend is that the normalized dissipation, ϵ^*, decreases as the vertical distance from the blade center line increases. Thus the maximum ϵ^* is at $r/R = 1.08$ and near $z = 0$. This is consistent with previous measurements. The magnitude of ϵ^* in this plot varies from approximately 5 to 35, demonstrating the significant concentration of dissipation in the impeller region.

The small-scale flow is anistropic, not only close to the blade tip, but in the entire region of investigation. Rao and Brodkey (1972) presented spectrum results exhibiting a $-5/3$ slope; however, the authors suggested that the existence of local isotropy does not directly follow from the $-5/3$ slope result. Instead, Rao and Brodkey (1972) suggested that full local isotropy would not be obtained until Re_λ is above 300. Komasawa et al. (1974) reported that the ratios $\sqrt{\overline{u_1^2}}/\sqrt{\overline{u_2^2}}$ were larger than one, and thus the turbulence was not strictly isotropic. The errors caused by the anisotropy were presumed small, following on suggestions by Hinze (1975). Energy spectra were reported and showed a $-5/3$ slope.

Hockey and Nouri (1996), carefully measuring the flow field around a PBT with LDV, found that in the discharge region, the turbulence was anisotropic. In the remaining regions of the tank, the turbulence was found to tend toward local isotropy.

Kresta and Wood's (1993) spectra showed a $-5/3$ slope, and a comparison of rms velocity components showed that the components in all three directions were "nearly equal." In this case, "nearly equal" was applied to a variation of 25–50%. Although this does not conclusively prove local isotropy, the authors state that the approximation is "supported" by this result and by the result that the integral time scales in all three directions are also comparable.

In the current study, the periodic component of the flow does not strongly affect estimates of dissipation. Figure 13 shows that the method of decomposition (including or not including the periodic component of velocity) affects the dissipation estimations only slightly in the very near blade region ($r/R < 1.2$). This agrees with Kresta and Wood's (1993) suggestion that the removal of the pseudoturbulence, or the periodic velocity field generated by the blades, did not significantly affect the final estimates of dissipation in a tank stirred by a PBT. It is possible that the periodic component has a higher effect in flows around a Rushton turbine; however, our results still show that the gradients used in estimating dissipation have a much higher effect on the calculations than the method of decomposition. The estimation of dissipation, which relies only on the $u_{1,1}$ component (ϵ_i), is consistently higher than the estimate that uses all measured components and isotropic assumptions for the other components (ϵ_{ii}).

Wu and Patterson (1989), however, emphasized the removal of the periodic component of the flow from the autocorrelation functions that formed their bases for estimating dissipation, among other turbulence quantities. A comparison of rms velocities in the impeller region, including and not including the periodic component, showed that there was a higher percentage difference between the three rms velocity components when the periodic component was not removed, especially close to the blade. When the periodic component was removed, the rms velocities for different directions varied by approximately 20%. The "corrected" (periodic component removed) spectrum appeared typical of a turbulence energy spectrum, and exhibited an approximately $-5/3$ slope.

The profiles of the rms velocities shown in Figure 15 indicate that generally the rms of u_r and u_z have similar magnitude. For the $r/R = 1.08$ position, the highest percentage difference between the components is approximately 40% and for the $r/R = 1.18$ position, the highest percentage difference is approximately 30%. The variation in magnitudes between rms components in Kresta and Wood's (1993) study was 25–50%. In their study, the components were considered equal even with this degree of variation, since "the three RMS components in highly anisotropic flows are expected to vary by up to 200%" (Kresta and Wood, 1993). The similarity of these components does not relate directly to the satisfaction of the isotropic assumptions when considering the ratios of mean square gradients.

Ratios of measured mean square gradients are plotted in Figure 16. The deviation from isotrophy in this plot is systematic. The highest deviation appears at 20 deg behind blade passage, just when the tip vortices are being shed from the blades. The highest degree of deviation from the isotropic value of 1 is approximately 80%, for the ratio of $\overline{u_{1,2}^2}/\overline{u_{2,1}^2}$ at 20 deg behind blade passage. This deviation indicates the significant anisotropy of the flow.

Experimentally, it is difficult to assess the true isotropy of the smallest scales. Antonia and Kim (1994) studied the degree to which local isotropy occurs at the smallest scales using direct numerical simulation (DNS) data. The primary data used in Antonia and Kim's study were from simulations of a turbulent channel flow, though the existence of small-scale isotropy from other simulations was also addressed. Antonia and Kim (1994) concluded that, at least for vorticity and temperature derivative spectra in a channel flow and representative homogeneous isotropic turbulence, homogeneous shear and a mixing layer, "isotropy appears to be satisfied at sufficiently large wave numbers, provided that the mean strain rate (suitably normalized) is sufficiently small." It should be noted, however, that significant anisotropy was seen in the homogeneous shear flow when the normalized strain rate, S^*, was too large. "In other words, the time scale associated with small scales is not sufficiently small compared to that of the mean shear rate" (Antonia and Kim, 1994). Considering the high concentration of δ^*, a variable used to quantify the magnitude of deformation rate attributed to mean velocity gradients in the impeller flow field in Stoots and Calabrese (1995), it is suggested that the small scales may indeed be anisotropic in the immediate vicinity of the Rushton turbine.

Estimating subgrid scale dissipation: Smagorinsky model

Based on a large-eddy simulation (LES) correction, the estimates of dissipation using PIV in this flow capture at least 70% of the true dissipation. Since the current PIV measurements are not resolved to the Kolmogorov scale, the Smagorinsky model is used to estimate the amount of dissipation contained in the unresolved scales. Discussion of this model in particular and LES methods in general may be found in Piomelli (1994). The subgrid scale dissipation is estimated as

$$\epsilon_{sgs} = -(C_s\Delta)^2|\bar{S}|^3, \tag{15}$$

where

$$\bar{S} = (2S_{ij}S_{ij})^{1/2}, \tag{16}$$

$$\bar{S}_{ij} = \frac{1}{2}\left(\frac{\partial \bar{u}_i}{\partial x_j} + \frac{\partial \bar{u}_j}{\partial x_i}\right), \tag{17}$$

$\Delta =$ grid spacing, and $C_s = 0.21 =$ the Smagorinksy constant.

The rate of dissipation by the mean field is

$$\epsilon_{\text{mean}} = \nu\left\{2\left(U_{1,1}^2 + U_{2,2}^2\right) + U_{1,2}^2 + U_{2,1}^2 + 2\left(U_{1,2}U_{2,1}\right)\right\}, \tag{18}$$

where $U = \langle \tilde{u} \rangle$. For the mean field averaged over all blade positions, U, the derivatives with respect to the circumferential direction (x_3) are zero. Two terms should be included in Eq. 18, namely, $U_{3,1}^2$ and $U_{3,2}^2$; however, these are not possible to calculate from 2-D data. Equation 18 is thus expected to slightly underestimate the amount of dissipation in the mean flow. Applying this equation to the mean field, U, ϵ_{mean} is estimated to be 0.0002 m^2/s^3, less than 10% of ϵ.

It is useful to compare the magnitude of the subgrid scale estimate, ϵ_{sgs}, to the most complete estimate using the "filtered" velocity field, namely ϵ_{ii} [decomposed using the traditional RANS method (Eq. 4)]. The ratio of $\epsilon_{ii}/(\epsilon_{ii} + \epsilon_{sgs})$ is consistently more than 0.7, indicating that the ϵ_{PIV} is capturing at least 70% of the true dissipation.

Summary and Conclusions

The strong coherence of the instantaneous vortices out to even 50° past blade passage is not accurately portrayed in either the phase-averaged, $\langle \tilde{u} | \theta \rangle$, or fully time-averaged, $\langle \tilde{u} \rangle$, velocity fields. Thus there is a loss of information if only the statistics of the mean field are used to model the flow, or if theories are drawn as to the structure of the flow based only upon mean field measurements.

The resolution of the PIV measurements is approximated to be 4–8 times the Kolmogorov scale, depending on the value of ϵ used to define the Kolmogorov scale. The physical size of the field of view containing 3,600 velocity vectors was 16.1 mm by 16.2 mm in the *r*- and *z*-directions, respectively. In order to resolve velocities at the Kolmogorov scale with current sensor technologies, the field of view in this particular test section needs to be 2 mm by 2 mm. Although this may be possible with constantly improving experimental apparatus, this smaller PIV field of view would be approaching the size of an LDV measurement volume containing only one velocity vector. For example, the LDA intersection volume in Yianneskis and Whitelaw (1993) was 1.035 mm by 0.167 mm. The use of this size PIV field of view could produce fully resolved instantaneous velocity gradients in the *r*- and *z*-directions, but there is still a loss of information in the third direction due to the two-dimensional nature of PIV. Of course, it might be possible to perform stereo PIV measurements at this resolution, though this experiment would be formidable.

The current results provide an estimate of dissipation based on spatially filtered velocity fields. Using a subgrid scale method based on LES techniques, we estimate that at least 70% of the true dissipation was captured in these calculations. The distributions of rms velocities, vorticity, and dissipation show the strong concentration of all quantities in the region of the shed tip vortices. The local dissipation in this area is estimated to be on the order of 10–25 times that in the bulk flow. The local dissipation is also found to decay with increasing distance from the blade in both the *r*- and *z*-directions, as expected. Subtraction of the periodic component does not affect the estimate of dissipation as much as the choice of symmetries (fully isotropic, axisymmetric, etc.) used for the actual calculation. The concentration of all statistical quantities in the region of the tip vortices emphasizes the importance of these structures as a major mixing mechanism in the stirred-tank flow.

At this resolution, the mean squared velocity gradients are found to be anisotropic. The ratios of mean square gradients (Figure 16) vary from 0.2 to 1.8, corresponding to deviations from isotropy up to 80%. Considering the magnitude of deformation rate attributed to mean velocity gradients in the impeller flow field and the fact that the Re_λ is less than 300, it is not surprising that the small scales may indeed be anistropic in the immediate vicinity of the Rushton turbine, and isotropic turbulence relations should not be used to estimate turbulent dissipation or other statistics dominated by the small scales.

Acknowledgments

This research was supported in part by a grant from the National Science Foundation, and one of the authors (K. V. S.) gratefully acknowledges fellowship support from Zonta International and the Department of Defense. We appreciate the interactions with K. C. Kim and S. Balachandar.

Literature Cited

Antonia, R. A., and J. Kim, "A Numerical Study of Local Isotropy of Turbulence," *Phys. Fluids*, **6**, 834 (1994).

Bakker, A., K. J. Meyers, R. W. Ward, and C. K. Lee, "The Laminar and Turbulent Flow Pattern of a Pitched Blade Turbine," *Trans. Inst. Chem. Eng.*, **74**, 485 (1996).

Cutter, L. A., "Flow and Turbulence in a Stirred Tank," *AIChE J.*, **12**, 35 (1966).

Desouza, A., and R. W. Pike, "Fluid Dynamics and Flow Patterns in Stirred Tanks with a Turbine Impeller," *Can. J. Chem. Eng.*, **50**, 15 (1972).

Ducoste, J. J., and M. M. Clark, "Turbulence in Flocculators: Effects of Tank Size and Impeller Type," *AIChE J.*, **43**, 328 (1997).

Gunkel, A. A., and M. E. Weber, "Flow Phenomena in Stirred Tanks: I. The Impeller Stream," *AIChE J.*, **21**, 931 (1975).

Hinze, J. O., *Turbulence*, McGraw-Hill, New York (1975).

Hockey, R. M., and J. M. Nouri, "Turbulent Flow in a Baffled Vessel Stirred by a 60 Degree Pitched Blade Impeller," *Chem. Eng. Sci.*, **51**, 4405 (1996).

Hunt, J. C. R., O. M. Phillips, and D. Williams, "Turbulence and Stochastic Processes: Kolmogorov's Ideas 50 Years On," *A. N. Commun. Issue Proc. R. Soc. London Ser. A*, The Royal Society, London (1991).

Keane, R. D., and R. J. Adrian, "Theory of Cross-Correlation Analysis of PIV Images," *Appl. Sci. Res.*, **49**, 191 (1992).

Komasawa, I., R. Kuboi, and T. Otake, "Fluid and Particle Motion in a Turbulent Dispersion: I. Measurement of Turbulence by Continual Pursuit of Tracer Particle Motion," *Chem. Eng. Sci.*, **29**, 641 (1974).

Kresta, S., "Turbulence in Stirred Tanks: Anisotropic, Approximate, and Applied," *Can. J. Chem. Eng.*, **76**, 563 (1998).

Kresta, S. M., and P. E. Wood, "The Flow Field Produced by a Pitched Blade Turbine: Characterization of the Turbulence and Estimation of the Dissipation Rate," *Chem. Eng. Sci.*, **48**, 1761 (1993).

Michelet, S., A. Kemoun, J. Mallet, and M. Mahouast, "Space-Time Velocity Correlations in the Impeller Stream of a Rushton Turbine," *Exp. Fluids*, **23**, 418 (1997).

Okamoto, Y., M. Nishikawa, and K. Hashimoto, "Energy Dissipation Rate Distribution in Mixing Vessels and Its Effects on Liquid-Liquid Dispersion and Solid-Liquid Mass Transfer," *Int. Chem. Eng.*, **21**, 88 (1981).

Piomelli, U., "Large-Eddy Simulation of Turbulent Flows," TAM

Rep. 767, Dept. of Theoretical and Applied Mechanics, Univ. of Illinois, Urbana-Champaign (1994).

Rao, M. A., and R. S. Brodkey, “Continuous Flow Stirred Tank Turbulence Parameters in the Impeller Stream,” *Chem. Eng. Sci.*, **27**, 137 (1972).

Reynolds, W. C., and A. K. M. F. Hussain, “The Mechanics of an Organized Wave in Turbulent Shear Flow. Part 3. Theoretical Models and Comparison with Experiments,” *J. Fluid Mech.*, **54**, 263 (1972).

Rutherford, K., S. M. S. Mahmoudi, K. C. Lee, and M. Yianneskis, “The Influence of Rushton Impeller Blade and Disk Thickness on the Mixing Characteristics of Stirred Vessels,” *Trans. Inst. Chem. Eng.*, **74**, 369 (1996).

Schäfer, M., M. Hofken, and F. Durst, “Detailed LDV-Measurements for Visualization of the Flow-Field Within a Rushton Turbine,” *Proc. Int. Symp. Applied Lasers to Fluid Mechanics*, Lisbon, Portugal, p. 8.4.1 (1996).

Sharp, K. V., K. C. Kim, and R. J. Adrian, “Dissipation Estimation Around a Rushton Turbine Using Particle Image Velocimetry,” *Proc. Int. Symp. Applied Lasers to Fluid Mechanics*, Lisbon, Portugal, p. 14.1.1 (1998).

Sharp, K. V., K. C. Kim, and R. J. Adrian, “A Comparison of Dissipation Estimation Methods in a Stirred Tank Using Particle Image Velocimetry,” *Proc. ASME/JSME Fluids Engineering Meeting*, San Francisco, CA (1999).

Sheng, J., H. Meng, and R. O. Fox, “Validation of CFD Simulations of a Stirred Tank Using Particle Image Velocimetry Data,” *Can. J. Chem. Eng.*, **76**, 611 (1998).

Soloff, S., and C. Meinhart, CLEANVEC: Particle Image Velocimetry Vector Validation Software, Private Communication (1998).

Stoots, C. M., and R. V. Calabrese, “Mean Velocity Field Relative to a Rushton Turbine Blade,” *AIChE J.*, **41**, 1 (1995).

Van’t Riet, K., and J. M. Smith, “The Trailing Vortex System Produced by Rushton Turbine Agitators,” *Chem. Eng. Sci.*, **30**, 1093 (1975).

Wu, H., and G. K. Patterson, “Laser-Doppler Measurements of Turbulent-Flow Parameters in a Stirred Mixer,” *Chem. Eng. Sci.*, **44**, 2207 (1989).

Yianneskis, M., Z. Popiolek, and J. H. Whitelaw, “An Experimental Study of the Steady and Unsteady Flow Characteristics of Stirred Reactors,” *J. Fluid Mech.*, **175**, 537 (1987).

Yianneskis, M., and J. H. Whitelaw, “On the Structure of the Trailing Vortices around Rushton Turbine Blades,” *Trans. Inst. Chem. Eng.*, **71**, 543 (1993).

Appendix: Data Files Available on Web Site

The following datafiles are available at http://ltcf.tam.uiuc.edu. All dimensional quantities are given in units of mm and seconds.

Filename	Column Labels
mean_totalu_0.txt	$r, z, \langle \tilde{u}_r, \tilde{u}_z \mid \theta = 0^\circ \rangle$
mean_totalu_10.txt	$r, z, \langle \tilde{u}_r, \tilde{u}_z \mid \theta = 10^\circ \rangle$
mean_totalu_20.txt	$r, z, \langle \tilde{u}_r, \tilde{u}_z \mid \theta = 20^\circ \rangle$
mean_totalu_30.txt	$r, z, \langle \tilde{u}_r, \tilde{u}_z \mid \theta = 30^\circ \rangle$
mean_totalu_40.txt	$r, z, \langle \tilde{u}_r, \tilde{u}_z \mid \theta = 40^\circ \rangle$
mean_totalu_50.txt	$r, z, \langle \tilde{u}_r, \tilde{u}_z \mid \theta = 50^\circ \rangle$
ens_urppuzpp_div_Vtipsq_0.txt	$r, z, \frac{\langle u_r'' u_z'' \mid \theta = 0^\circ \rangle}{V_{\rm tip}^2}$
ens_urppuzpp_div_Vtipsq_10.txt	$r, z, \frac{\langle u_r'' u_z'' \mid \theta = 10^\circ \rangle}{V_{\rm tip}^2}$
ens_urppuzpp_div_Vtipsq_20.txt	$r, z, \frac{\langle u_r'' u_z'' \mid \theta = 20^\circ \rangle}{V_{\rm tip}^2}$
ens_urppuzpp_div_Vtipsq_30.txt	$r, z, \frac{\langle u_r'' u_z'' \mid \theta = 30^\circ \rangle}{V_{\rm tip}^2}$
ens_urppuzpp_div_Vtipsq_40.txt	$r, z, \frac{\langle u_r'' u_z'' \mid \theta = 40^\circ \rangle}{V_{\rm tip}^2}$
ens_urppuzpp_div_Vtipsq_50.txt	$r, z, \frac{\langle u_r'' u_z'' \mid \theta = 50^\circ \rangle}{V_{\rm tip}^2}$
ens_urrms_div_Vtip_0.txt	$r, z, \frac{(\langle u_r''^2 \mid \theta = 0^\circ \rangle)^{1/2}}{V_{\rm tip}}$
ens_urrms_div_Vtip_10.txt	$r, z, \frac{(\langle u_r''^2 \mid \theta = 10^\circ \rangle)^{1/2}}{V_{\rm tip}}$
ens_urrms_div_Vtip_20.txt	$r, z, \frac{(\langle u_r''^2 \mid \theta = 20^\circ \rangle)^{1/2}}{V_{\rm tip}}$
ens_urrms_div_Vtip_30.txt	$r, z, \frac{(\langle u_r''^2 \mid \theta = 30^\circ \rangle)^{1/2}}{V_{\rm tip}}$
ens_urrms_div_Vtip_40.txt	$r, z, \frac{(\langle u_r''^2 \mid \theta = 40^\circ \rangle)^{1/2}}{V_{\rm tip}}$
ens_urrms_div_Vtip_50.txt	$r, z, \frac{(\langle u_r''^2 \mid \theta = 50^\circ \rangle)^{1/2}}{V_{\rm tip}}$
ens_uzrms_div_Vtip_0.txt	$r, z, \frac{(\langle u_z''^2 \mid \theta = 0^\circ \rangle)^{1/2}}{V_{\rm tip}}$
ens_uzrms_div_Vtip_10.txt	$r, z, \frac{(\langle u_z''^2 \mid \theta = 10^\circ \rangle)^{1/2}}{V_{\rm tip}}$
ens_uzrms_div_Vtip_20.txt	$r, z, \frac{(\langle u_z''^2 \mid \theta = 20^\circ \rangle)^{1/2}}{V_{\rm tip}}$
ens_uzrms_div_Vtip_30.txt	$r, z, \frac{(\langle u_z''^2 \mid \theta = 30^\circ \rangle)^{1/2}}{V_{\rm tip}}$
ens_uzrms_div_Vtip_40.txt	$r, z, \frac{(\langle u_z''^2 \mid \theta = 40^\circ \rangle)^{1/2}}{V_{\rm tip}}$
ens_uzrms_div_Vtip_50.txt	$r, z, \frac{(\langle u_z''^2 \mid \theta = 50^\circ \rangle)^{1/2}}{V_{\rm tip}}$
ens_vort_0.txt	$r, z, \langle \omega \mid \theta = 0^\circ \rangle$
ens_vort_10.txt	$r, z, \langle \omega \mid \theta = 10^\circ \rangle$
ens_vort_20.txt	$r, z, \langle \omega \mid \theta = 20^\circ \rangle$
ens_vort_30.txt	$r, z, \langle \omega \mid \theta = 30^\circ \rangle$
ens_vort_40.txt	$r, z, \langle \omega \mid \theta = 40^\circ \rangle$
ens_vort_50.txt	$r, z, \langle \omega \mid \theta = 50^\circ \rangle$

Manuscript received Nov. 29, 1999, and revision received Oct. 2, 2000.